Contents lists available at ScienceDirect

Transactions of Nonferrous Metals Society of China

36(2026) 183−202

www.tnmsc.cn

Unanticipated strengthening of Cu−19Ni−6Cr−7Mn alloy achieved by synergistic effect of spinodal decomposition and multiscale precipitation

Shao-lin LI [a,*], Ying-ying ZHU [a], Xiu-hua GUO [a], Qiang-song WANG [b,c], Wen-ming SUN [a], Ke-xing SONG [a,b,**]

[a] Henan Key Laboratory of Non-ferrous Materials Science and Processing Technology, School of Materials Science and Engineering, Henan University of Science and Technology, Luoyang 471023, China;

[b] Henan Key Laboratory of Advanced Conductor Materials, Institute of Materials, Henan Academy of Sciences, Zhengzhou 450046, China;

[c] GRIMAT Engineering Institute Co., Ltd., Beijing 101407, China

Abstract: The microstructural evolution of Cu−19Ni−6Cr−7Mn alloy during aging treatment was investigated. After aging for 120 min at 500 °C, the alloy exhibited excellent mechanical properties, including a tensile strength of 978 MPa and an elastic modulus of 145.8 GPa. After aging for 240 min at 500 °C, the elastic modulus of the alloy reached 149.5 GPa, which was among the highest values reported for Cu alloys. It was worth mentioning that the tensile strength increased rapidly from 740 to 934 MPa after aging for 5 min at 500 °C, which was close to the maximum tensile strength (978 MPa). Analysis of the underlying strengthening mechanisms and phase transformation behavior revealed that the Cu−19Ni−6Cr−7Mn alloy underwent spinodal decomposition and DO_{22} ordering during the first 5 min of aging at 500 °C, and $L1_2$ ordered phases and bcc-Cr precipitates appeared. Therefore, the enhanced mechanical properties of the Cu−19Ni−6Cr−7Mn alloy can be attributed to the stress field generated by spinodal decomposition and the presence of nanoscale ordered phase and Cr precipitates.

Keywords: Cu−Ni−Cr−Mn alloy; mechanical properties; nanoscale precipitates; spinodal decomposition; elastic modulus

1 Introduction

Copper alloys are widely used in marine engineering and the electrical and electronics industries owing to their excellent mechanical properties, electrical and thermal conductivities, and corrosion resistance [1−3]. Copper−beryllium (Cu−Be) alloys are among the most extensively utilized copper-based elastic alloys. Nevertheless, they have obvious limitations. In particular, many beryllium compounds, such as beryllium oxides, are highly toxic, which limits the production and application of the Cu−Be alloy. In recent years, researchers have developed new high-elasticity Cu alloys as alternatives to the Cu−Be alloy, such as Cu−Ni−Sn [4,5], Cu−Ni−Al [6,7], Cu−Ni−Mn [8,9], Cu−Ti [10,11], and Cu−Ni−Cr [12]. Cu−Ni−Cr alloys are novel Cu-based elastic alloys with excellent mechanical strength, elastic modulus, and corrosion resistance. Cu−Ni−Cr alloys are typical spinodal decomposition alloys. During the aging process, Cu−Ni−Cr alloys are synergistically strengthened by the spinodal decomposition, coherent ordered phases, and a large proportion of nanoscale Cr precipitates [12,13]. In summary,

---

Corresponding author: [*]Shao-lin LI, Tel: +86-15194561655, E-mail: lsl0379@haust.edu.cn;
[**]Ke-xing SONG, Tel: +86-13707697980, E-mail: kxsong@haust.edu.cn

https://doi.org/10.1016/S1003-6326(25)66957-3

Received 8 April 2024; accepted 14 February 2025

Cu−Ni−Cr alloys have great potential in the development of high-strength, high-elasticity Cu alloys.

The investigations into the phase transition behavior of Cu−Ni−Cr alloys have mainly focused on the effects of aging treatment on the mechanical properties and wavelength of spinodal decomposition [14−16]. CHOU et al [13] subjected Cu−31.6Ni−1.7Cr to an aging treatment and observed significant morphological changes in the precipitation-induced spinodal decomposition. Specifically, they found that the structural transformation sequence during spinodal decomposition was cuboid → rod → sheet (raft). LI et al [12] studied the microstructural evolution of $Cu_x[Ni_3Cr_1]$ (x=1, 2, 3, 4, 5, 7, 9, and 12) with different compositions. As x increased, the tensile strength of the aged alloy gradually decreased from 818 to 484 MPa. Aged Cu−0.19Ni−0.27Cr exhibited remarkable stress relaxation resistance, which was attributed to the combined effects of dislocation strengthening, second-phase strengthening, spinodal decomposition, and ordered coexistence [2]. Moreover, after cold rolling, Cu−1.16Ni−0.36Cr exhibited a tensile strength of 536.1 MPa. Notably, the precipitation of Ni_3Cr_7 significantly increased the high-temperature resistance of the alloy [17,18]. Advancements in high-tech industries such as electronics have increased the demand for Cu alloys with enhanced mechanical properties. Therefore, this study aimed to satisfy the performance requirements of high-strength, high-elasticity Cu alloys by further optimizing the mechanical properties (e.g., tensile strength) of Cu−Ni−Cr alloys using different aging parameters.

Understanding the phase transition pathways during aging is beneficial for the design and processing of multiphase materials, since it allows the microstructure to be tailored to control the mechanical properties for technical applications [19,20]. Therefore, studies are required to investigate the formation and evolution of spinodal decomposition structures and nanoprecipitates during alloy aging and their effects on the mechanical properties of alloys. Previous studies have shown that Cu−15Ni−8Sn undergoes spinodal decomposition during aging, which leads to the formation of periodic structures within the alloy. In particular, during prolonged aging, spinodal decomposition leads to the gradual formation of DO_{22} and $L1_2$ ordered phases, which improve the mechanical properties of the alloy through complete coherence with the matrix [21]. The precipitation sequence in Cu−3Ti−1Cr alloy aged at 500 °C was also investigated, indicating that the β'-Cu_4Ti phase is formed through spinodal decomposition. Moreover, the strengthening effect of Cr on the matrix is mainly induced by the formation of a coarse Cr phase, a Ti−Cr phase and nanosized Cr precipitates [22]. Alloying elements are widely used to increase the strength of alloys. When Cu−Ni−Si−Cr alloys are aged at 500 °C, their mechanical properties are improved because of the formation of three precipitated phases: β-Ni_3Si, δ-Ni_2Si, and rich (Ni,Cr,Si) phases [23]. During aging process of Cu−20Ni−20Mn, numerous finely-dispersed NiMn phases, with dimensions of 2−3 nm, precipitate from the matrix. These nanoscale NiMn phases possess an $L1_2$ crystal structure and have complete coherence with the surrounding matrix, which significantly improves the mechanical properties of the Cu−20Ni−20Mn alloy [24].

In this study, we examined the spinodal decomposition and multiscale precipitate evolution in the Cu−19Ni−6Cr−7Mn alloy, an Mn-enhanced Cu−Ni−Cr alloy. Aging time and temperature significantly affect phase transformations and precipitation. Therefore, the primary objective of this study was to explore the effects of various aging parameters on the microstructure and mechanical properties of Cu−19Ni−6Cr−7Mn alloy, and thereby elucidate the underlying phase transformation behavior and the strengthening mechanisms. The results provide theoretical insights into the design and application of high-strength, high-elasticity Cu−19Ni−6Cr−7Mn alloy.

2 Experimental

2.1 Preparation of Cu−19Ni−6Cr−7Mn alloy

Cu−19Ni−6Cr−7Mn alloy was prepared using pure Cu (99.99 wt.%), electrolytic Mn (99.99 wt.%), and Ni−Cr intermediate alloy (x(Ni)/x(Cr)=3) as the raw materials. The chemical compositions of the ingot are given in Table 1. The alloy preparation process was as follows. A graphite crucible was heated using a resistance wire. After preheating, the pure Cu and Ni−Cr intermediate alloys were placed in the crucible and melted. Next, electrolytic Mn was added to the crucible. Charcoal was used as a covering agent to isolate the alloy from the air to reduce oxidation. Once all the raw materials melted, the melt was poured into a high-purity graphite crucible (80 mm × 200 mm) to complete the casting process. The melting temperature was 1200−1300 °C, and the pouring temperature was controlled at 1100−1150 °C. The ingot was homogenized in an electric heating furnace (5X−12−11) for 12 h at 1050 °C. After holding for 1 h at 980 °C, the ingot was forged using an air hammer (C41-750), which produced an 8 mm-thick strip. The strip was processed for 3 h at 900 °C through solution treatment and 90% cold deformation. Subsequently, the alloy strips were subjected to isothermal aging treatments across a temperature range of 400−700 °C with controlled holding durations. The processing methodology and heat-treatment parameters are illustrated in Fig. 1. The microstructural evolution and mechanical properties of the Cu−19Ni−6Cr−7Mn alloy samples aged under different conditions were analyzed.

Table 1 Chemical composition of Cu−19Ni−6Cr−7Mn alloy (wt.%)

Cu	Ni	Cr	Mn
Bal.	19.34	5.74	7.18

2.2 Microstructural characterization

The microstructural evolution of the Cu−19Ni−6Cr−7Mn alloy during the aging process was investigated. First, the alloy samples were pre-ground, polished, and etched using a mixture of HNO_3, CH_3COOH, and H_2O (volume ratio of 3:3:4). Subsequently, microstructures of the alloy were observed and microstructural changes were identified through scanning electron microscopy (SEM, JSM−IT100). Field-emission SEM (JSM−7800F, JEOL Ltd.) conducted at an acceleration voltage of 20 kV and a sample tilt of 70° was performed to observe the surface microstructure and elemental distribution of the alloy samples. X-ray diffraction (XRD; D8 Advanced analyzer, Bruker) conducted at a voltage of 40 kV, current of 40 mA, scanning speed of 0.2 s per step, and scanning range of 35°−100° was carried out for phase identification. The cold-rolled and aged samples were characterized through transmission electron microscopy (TEM; FEI Talos F200X, Thermo Fisher Scientific Inc.). The TEM samples were prepared by grinding them to a thickness of 30 μm, followed by immersing the disks with a diameter of 3 mm into an electrolyte solution containing perchloric acid and ethanol.

2.3 Mechanical and electrical performance measurements

The microhardness of the alloy was evaluated using a digital microhardness tester (HVS−1000A) and a load of 9.8 N was applied for 10 s. The measurement was conducted five times for each sample, and the data were averaged to obtain the representative results. The conductivity of the alloy was assessed using a digital conductivity meter (Sigma 2008B1). The measurement was conducted ten times for each sample, and the data were averaged to obtain the representative results. The dog-bone-shaped tensile specimens with dimensions of 65 mm × 15 mm were cut from the plane along the rolling direction of each strip through electrical discharge machining. The computer-controlled electronic universal testing

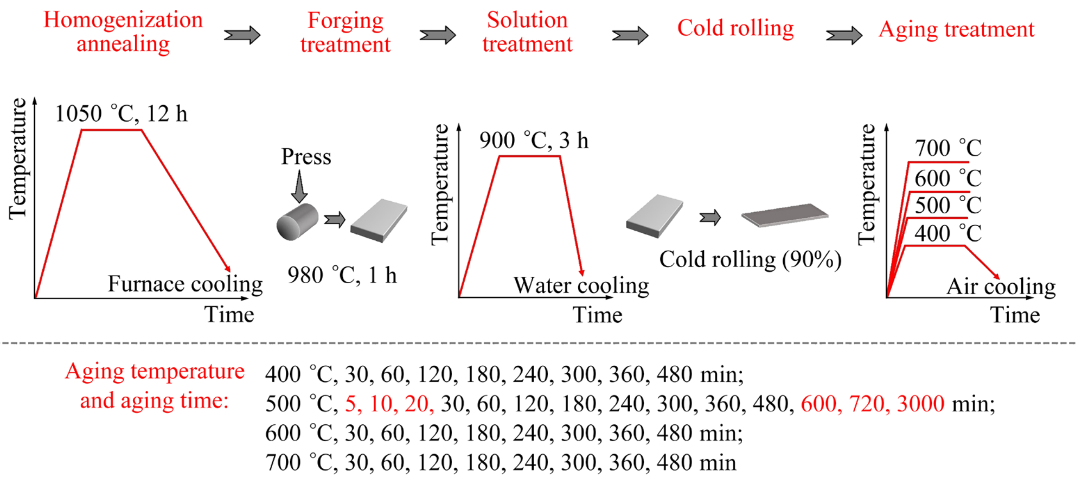

Fig. 1 Flow chart of machining and heat treatment of Cu−19Ni−6Cr−7Mn alloy

machine (WDW−100) was operated at a fixed rate of 1 mm/min. Three parallel samples were tested at room temperature (~25 °C) for each group to ensure the accuracy and reliability of the measurements.

3 Experimental results

3.1 Mechanical and electrical properties

Figure 2(a) shows the hardness as a function of aging time for the Cu−19Ni−6Cr−7Mn alloy aged at 400, 500, 600, and 700 °C. The hardness of the alloy aged at 400 and 500 °C initially increased and then decreased as the aging time increased. The hardness exceeded that of the cold-rolled alloy (HV 311.7), which indicates a substantial age-hardening effect. By contrast, the hardness of the alloy aged at 600 and 700 °C decreased to a value lower than that of the cold-rolled alloy. The hardness of the alloy aged at 500 °C was significantly higher than that of the samples aged at other temperatures. The alloy aged at 500 °C achieved its peak hardness (HV 375.5) after 120 min, while that aged at 400 °C reached its peak hardness (HV 370.8) after 300 min. This indicates that the peak aging time decreased as the aging temperature increased.

Figure 2(b) shows the conductivity as a function of aging time for the Cu−19Ni−6Cr−7Mn alloy aged at 400, 500, 600, and 700 °C. The conductivity of the alloy increased as the aging time increased. Notably, the conductivity of the Cu−19Ni−6Cr−7Mn alloy aged at 500 °C was significantly higher than that of the alloys aged at other temperatures. After aging for 30 min at 500 °C, the conductivity of the Cu−19Ni−6Cr−7Mn alloy increased rapidly from 2.74% (IACS) to 3.74% (IACS). The maximum conductivity of 3.83% (IACS) was observed for the alloy aged at 500 °C for 120 min.

Figure 2(c) shows the ultimate tensile strength (UTS) as a function of aging time for the Cu−19Ni−6Cr−7Mn alloy aged at 400, 500, 600, and 700 °C. For the Cu−19Ni−6Cr−7Mn alloys aged at 400 and 500 °C, the tensile strength initially increased and then decreased as the aging time increased; their tensile strength values surpassed that of the cold-rolled alloy (740 MPa). For the alloys aged at 600 °C, the tensile strength increased briefly and

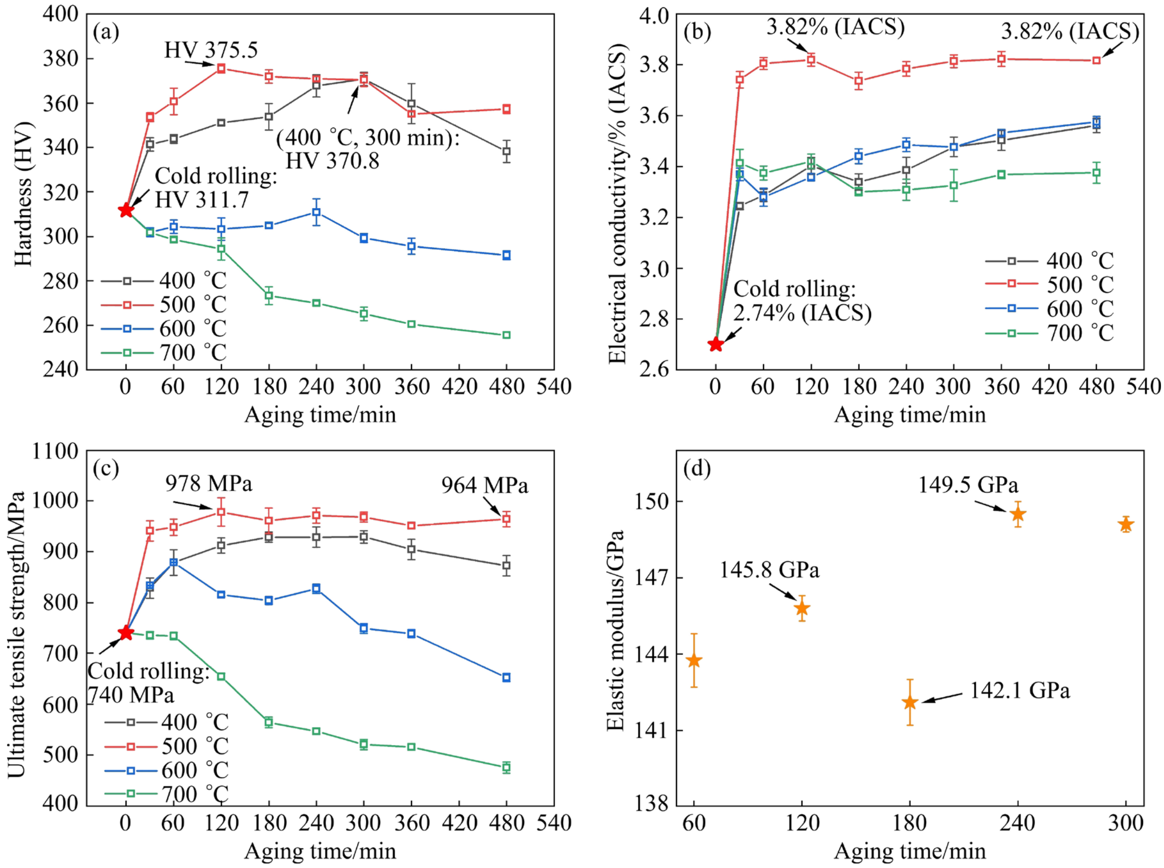

Fig. 2 Mechanical and electrical properties of Cu−19Ni−6Cr−7Mn alloys after aging: (a) Hardness; (b) Electrical conductivity; (c) Ultimate tensile strength; (d) Elastic modulus (aged at 500 °C)

then decreased as the aging time increased. For the alloys aged at 700 °C, the tensile strength was lower than that of the cold-rolled alloy and decreased as the aging time increased. Over-aging at 600 and 700 °C degraded the properties of the alloy. By contrast, the tensile strength of the alloys aged at 500 °C greatly exceeded that of the samples aged at other temperatures. The time required to reach the peak tensile strength decreased as the aging temperature increased. The tensile strength of the alloy aged at 500 °C remained stable over time and did not decrease. Figure 2(d) shows the elastic modulus of the Cu−19Ni−6Cr−7Mn alloys aged at 500 °C for 60−300 min. The elastic modulus of the alloy was 143.8 GPa after 60 min, and it peaked at 149.5 GPa after 240 min.

As shown in Fig. 2, the tensile strength and other mechanical properties of the Cu−19Ni−6Cr−7Mn alloys aged at 500 °C remained stable with no significant decline as the aging time increased. Therefore, additional short-term (5, 10, and 20 min) and long-term (600, 720, and 3000 min) aging tests were conducted at 500 °C. Figure 3 shows the mechanical properties and electrical conductivity of the Cu−19Ni−6Cr−7Mn alloys aged at 500 °C for different time. Figures 3(a, b) show the tensile and yield strengths over time for the Cu−19Ni−6Cr−7Mn alloys aged at 500 °C. Both strength values showed similar trends. After aging for 5 min at 500 °C, the tensile strength of the alloy increased from 740 MPa (cold-rolled) to 934 MPa, which was only 4.5% less than the maximum tensile strength of 978 MPa. After aging for 600, 720, and 3000 min at 500 °C, the tensile strength values of the Cu−19Ni−6Cr−7Mn alloy were 951, 948, and 800 MPa, respectively. After aging for 3000 min at 500 °C, the tensile strength of the aged sample remained higher than that of the cold-rolled alloy. These results indicate that aging for 5 min at 500 °C significantly improved the strength of the Cu−19Ni−6Cr−7Mn alloy. Moreover, the properties of the alloy remain stable upon extended aging, and they are highly resistant to softening [25]. Figures 3(c, d) show the hardness and conductivity over time for the Cu−19Ni−6Cr−7Mn alloy aged at 500 °C. The hardness of the alloys initially increased, peaked at HV 375.5 after aging for 120 min, and decreased. Moreover, the electrical conductivity of the alloy initially increased and then stabilized as the aging time increased.

3.2 Microstructural evolution

3.2.1 XRD analysis

The XRD results reveal the evolution of the precipitated phase during the aging process. Figure 4 shows the XRD patterns for the Cu−19Ni−6Cr−7Mn alloy aged at 400, 500, 600, and 700 °C for different aging time. The diffraction peaks of the alloy after cold rolling mainly correspond to a Cu matrix. After aging, the peak

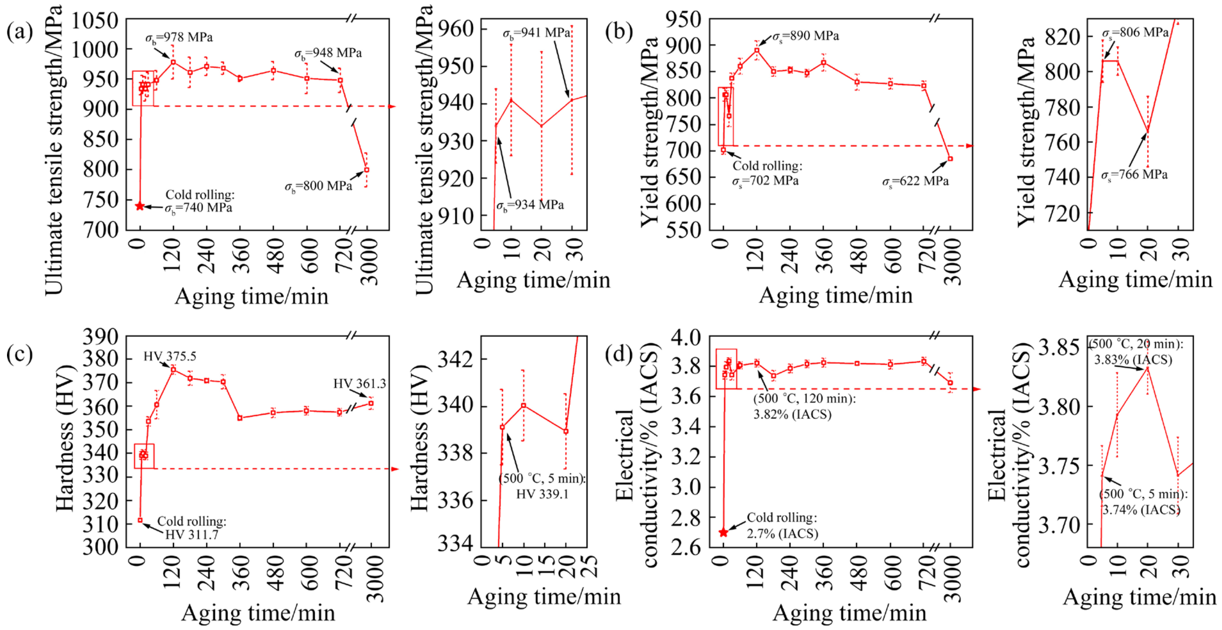

Fig. 3 Mechanical and electrical properties of Cu−19Ni−6Cr−7Mn alloys aged at 500 °C: (a) Ultimate tensile strength; (b) Yield strength; (c) Hardness; (d) Electrical conductivity

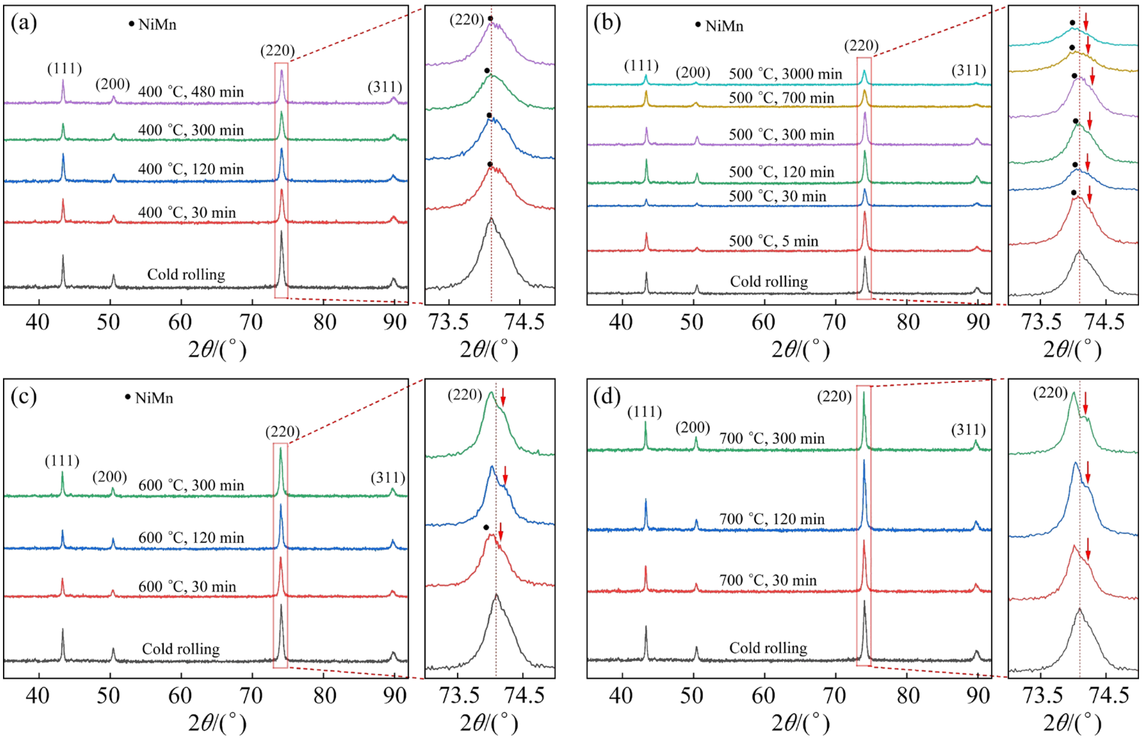

Fig. 4 XRD patterns of aged Cu−19Ni−6Cr−7Mn alloys: (a) 400 °C; (b) 500 °C; (c) 600 °C; (d) 700 °C

broadened owing to the precipitation of the Ni_3Mn precipitates [26]. As shown in Figs. 4(a, b), the diffraction peaks corresponding to the Ni_3Mn precipitates appeared in the patterns of the Cu−19Ni−6Cr−7Mn alloy aged at 400 and 500 °C. The lattice parameters of the Ni_3Mn precipitates closely matched those of the Cu matrix, which caused their diffraction peaks to partially overlap (Table 2); diffraction peak broadening is an important feature of spinodal decomposition [22,27]. The diffraction peaks of the Cu−19Ni−6Cr−7Mn alloy aged at 400 °C shifted slightly to the right as the aging time increased owing to the gradual precipitation of solute atoms reducing the interplanar spacing of the matrix. When the aging temperature increased to 600 and 700 °C, the diffraction peak corresponding to the Ni_3Mn precipitates disappeared, as shown in Figs. 4(c, d), and the remaining peaks mainly corresponded to the Cu matrix and side bands. Prolonged aging shifted the Cu diffraction peak to a lower 2θ value, which indicates that the Ni_3Mn precipitates precipitated in the matrix and that the crystal plane spacing increased.

Table 2 Comparison of information in PDF cards of Cu and Ni_3Mn

Cu (PDF# 00-001-1241)			Ni_3Mn (PDF# 04-003-3877)		
2θ/(°)	*d*/nm	(*hkl*)	2θ/(°)	*d*/nm	(*hkl*)
43.4716	0.205	(111)	43.5945	0.207	(111)
50.3734	0.181	(200)	50.7787	0.180	(200)
73.9952	0.128	(220)	74.6547	0.127	(220)
89.9309	0.109	(311)	90.6373	0.108	(311)

3.2.2 SEM analysis

Figure 5 shows the SEM and energy-dispersive X-ray spectroscopy (EDS) elemental distribution images of the Cu−19Ni−6Cr−7Mn alloy aged for 120 min at 500 °C. As shown in Fig. 5(a), two shapes of precipitates appeared in the matrix. The long-strip precipitates resulted from particle elongation along the rolling direction after 90% cold deformation. Even after aging for 120 min at 500 °C, the precipitates did not exhibit recovery. The EDS elemental distributions corresponding to Fig. 5(a), shown in Figs. 5(b_1−b_4), indicate that Cr segregation occurred in the precipitate regions. A magnified image of the precipitates in Fig. 5(a) is shown in Fig. 5(c). Point-scan results indicate that the precipitates and matrix consisted of $Cu_{7.6}Ni_{24.2}Cr_{63.7}Mn_{4.5}$ and $Cu_{67.7}Ni_{22.5}Cr_{2.1}Mn_{7.7}$, respectively. Line-scan results, shown in Fig. 5(d), reveal that the precipitates had high Cr content. The low solubility of Cr in Cu and the high Cr content

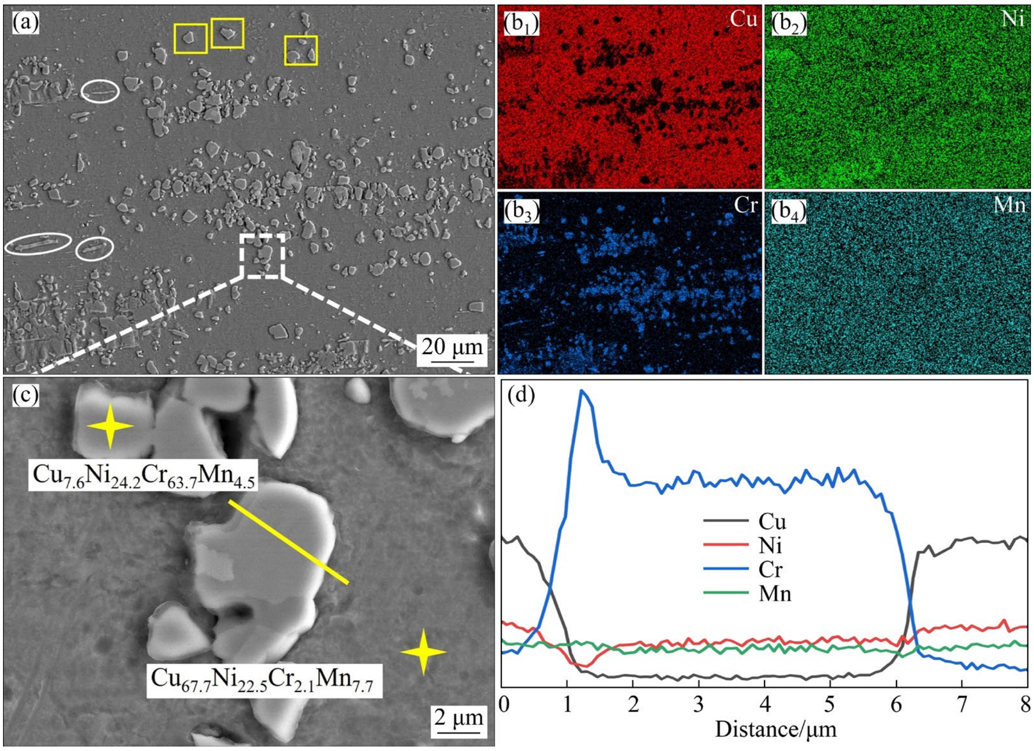

Fig. 5 SEM and EDS element distribution images of Cu−19Ni−6Cr−7Mn alloy aged at 500 °C for 120 min: (a) SEM image; (b_1−b_4) Element distribution maps in (a); (c) Partial enlargement of SEM image; (d) Element distribution result of line sweep in (c)

of the alloy in this study caused preferential Cr precipitation during cooling, which led to the formation of Cr-rich particles in the matrix [22]. Mn, a solid-solution constituent, was uniformly distributed in the Cu matrix, which significantly affected the movement of dislocations and grain boundaries [28].

3.2.3 TEM analysis

Dislocation intersections and entanglements during movement lead to dislocation pile-ups, which impede dislocation motion and increase the strength of alloys. The TEM images of the cold-rolled Cu−19Ni−6Cr−7Mn alloy are shown in Fig. 6. The bright-field (BF) image of the matrix and selected area electron diffraction (SAED) pattern in Fig. 6(a) indicated that the Cu matrix had a face-centered cubic (FCC) structure. Moreover, the inverse fast Fourier transform (IFFT) image in Fig. 6(b) showed numerous dislocations. Cold rolling typically increased the number of defects in the Cu−19Ni−6Cr−7Mn alloys. This was evident in Fig. 6(c), wherein the substantial dislocation entanglement and accumulation were observed because of deformation. Moreover, larger particles were also observed, as could be seen in the BF image and EDS elemental point-scan results for these particles ($Cu_{69.59}Ni_{21.33}Cr_{1.96}Mn_{7.09}$ and $Cu_{5.93}Ni_{23}Cr_{65.45}Mn_{5.52}$) in Figs. 6(d, e). According to the "Image" measurement software, the Cr-rich particles in Fig. 6(e) had a diameter of 299 nm. The calibration results for the precipitated particles in Fig. 6(e) are shown in Fig. 6(f). The Cr precipitations possessed a body-centered cubic bcc structure with a crystal face spacing of 0.203 nm, as shown in the IFFT and SAED images.

The TEM images of the Cu−19Ni−6Cr−7Mn alloy aged for 5 min at 500 °C are shown in Fig. 7. The Cu−19Ni−6Cr−7Mn alloy contained large Cr precipitates, numerous dislocation lines, dislocation tangles, and dislocation pile-ups, as shown in Figs. 7(a, b). The EDS results (Figs. 7(b_1−b_4)) indicated that the average size was approximately 31.4 nm. The BF images of the Cr precipitations are presented in Figs. 7(c, d), and the high-resolution TEM (HRTEM) images of the precipitated phase are shown in Fig. 7(e). The fast Fourier transform (FFT) model in Fig. 7(e) showed that the precipitated phase was the bcc-Cr precipitates and the $(01\bar{1})_{Cr}$ crystal plane spacing was 0.203 nm. The Cu matrix contained the bcc-Cr

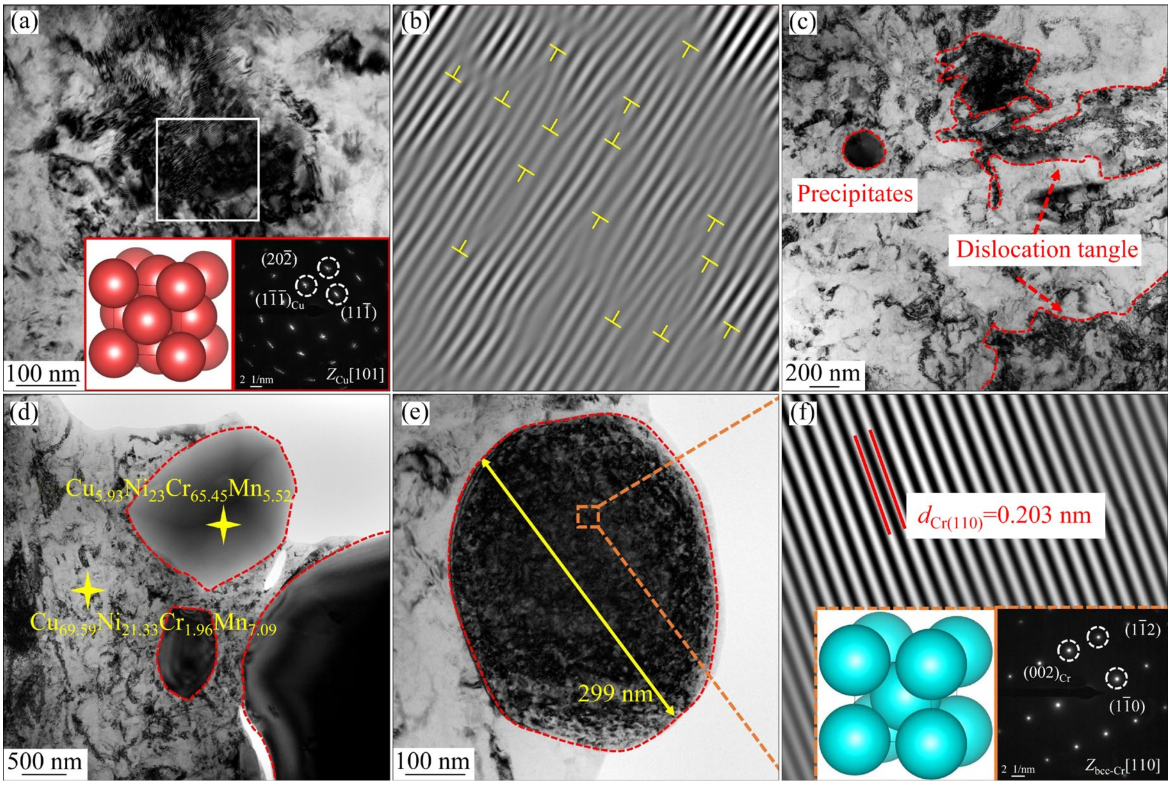

Fig. 6 TEM analysis of cold-rolled Cu−19Ni−6Cr−7Mn alloy: (a) BF image of matrix; (b) SAED image of red box area in (a); (c−e) BF images of precipitates; (f) SAED image of precipitated particles in (e)

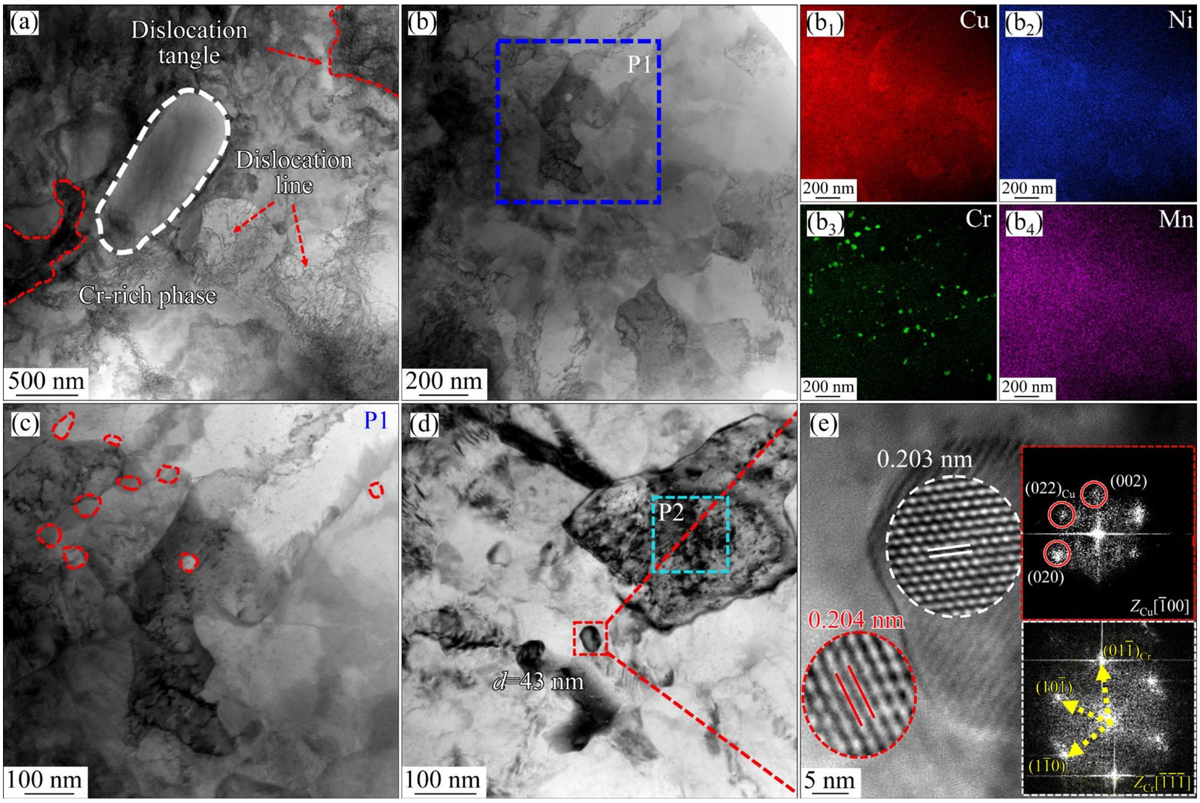

Fig. 7 TEM analysis of Cu−19Ni−6Cr−7Mn alloy aged at 500 °C for 5 min: (a, b, d) BF images; (b_1−b_4) Element distribution in (b); (c) Local enlarged view of P1 region in (b); (e) HRTEM image of precipitates in (d)

precipitates and the $(110)_{\mathrm{Cu}}$ crystal face spacing was 0.204 nm. The mismatch (σ) between the bcc-Cr precipitates and the Cu matrix crystal faces can be expressed as

$$\sigma=\frac{2(d_\alpha-d_\beta)}{d_\alpha+d_\beta}=\frac{2\times(0.204-0.203)}{0.204+0.203}\times 100\%=0.64\%<5\% \tag{1}$$

where d_α and d_β are the crystal face spacings of $(01\bar{1})_{\text{bcc-Cr}}$ precipitates and $(110)_{\mathrm{Cu}}$ parallel crystal faces, respectively. The results showed that the interface between the bcc-Cr precipitates and Cu matrix is coherent. The orientation relationship between the Cu matrix and Cr precipitates was found to be $(01\bar{1})_{\mathrm{Cr}}//(002)_{\mathrm{Cu}}$, $[\bar{1}\bar{1}\bar{1}]_{\mathrm{Cr}}//[\bar{1}00]_{\mathrm{Cu}}$.

The TEM images of Region P2 (in Fig. 7(d)) for the Cu−19Ni−6Cr−7Mn alloy aged for 5 min at 500 °C revealed needle-like precipitates, as shown in Fig. 8(a). The FFT diagrams (Figs. 8(a_1, a_2)) showed additional superlattice diffraction spots and the standard diffraction spots corresponding to the $(100)_{\mathrm{Cu}}$ matrix. IFFT diagrams corresponding to the yellow and green boxes in the HRTEM image (in Fig. 8(a)) are shown in Figs. 8(b, c), respectively. The FFT diagrams in Figs. 8(b_1, c_1) showed the $L1_2$ ($Pm\bar{3}m$, a=0.359 nm) and DO_{22} ($I4/mmm$, a=0.377 nm, c=0.724 nm) phases. The superlattice diffraction spots corresponding to the DO_{22} ordered phase confirmed that spinodal decomposition occurred and suggested that the spinodal decomposition structure of the alloy underwent an ordered transformation [29].

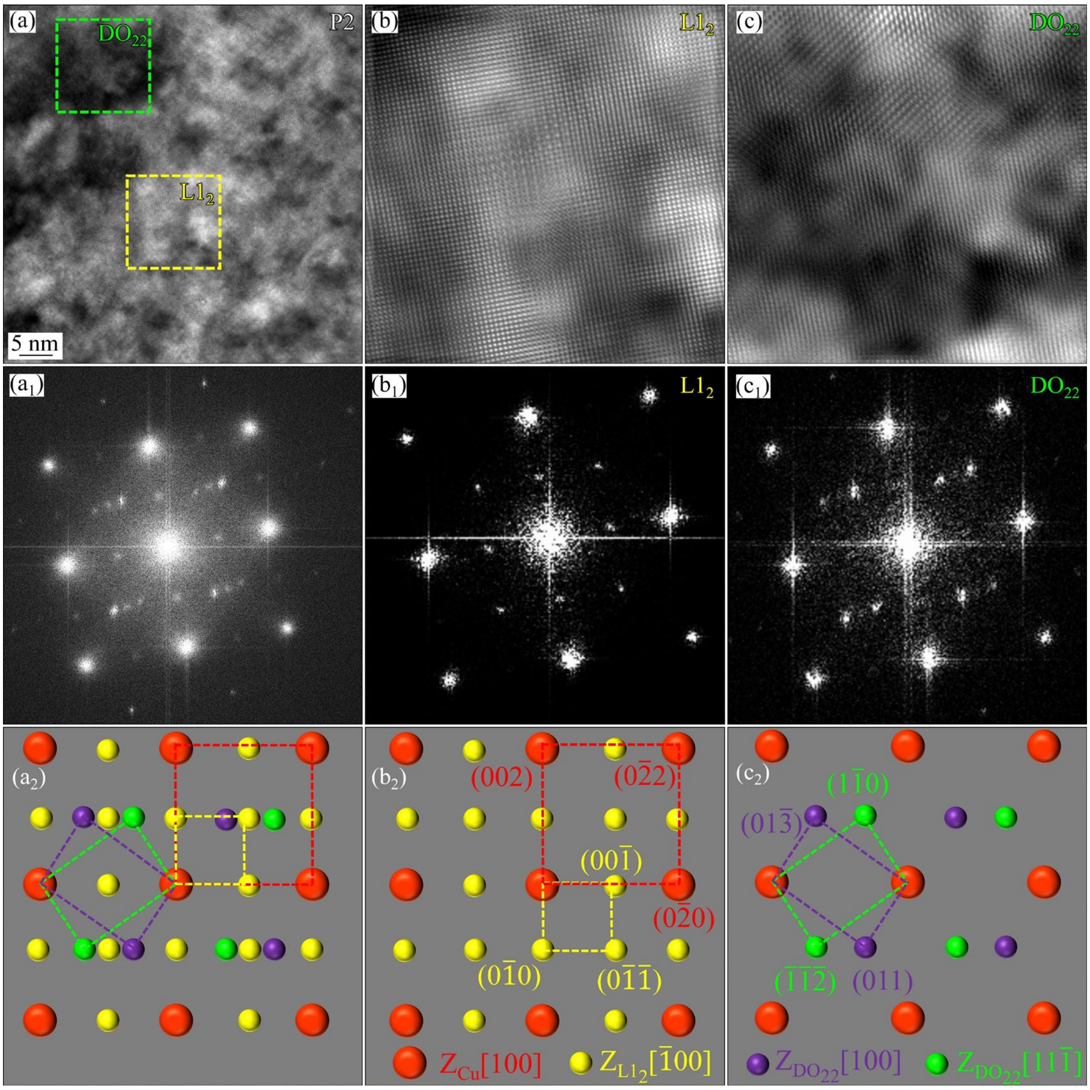

Fig. 8 Detailed TEM analysis of Cu−19Ni−6Cr−7Mn alloy aged at 500 °C for 5 min showing $L1_2$ and DO_{22} phases: (a) HRTEM image of Region P2 in Fig. 7(d); (a_1, a_2) FFT diagram of (a) and calibration diagram corresponding to FFT diagram, respectively; (b, c) Enlarged views of corresponding area in (a); (b_1, b_2, c_1, c_2) FFT diagrams and calibration diagrams corresponding to FFT diagram in (b) and (c), respectively

IFFT transformation and crystal face spacing measurement were performed using Fig. 8(b_1); the results are shown in Fig. 9. As shown in Figs. 9(b, c), the crystal face spacings of $L1_2$ ordered phases (100) and (110) were $d_{(100)}$= 0.353 nm and $d_{(110)}$=0.257 nm, respectively. These values were consistent with the lattice spacing of Ni_3Mn (XRD data in Fig. 4 and Table 2). Therefore, the $L1_2$ diffraction spots in the Cu−19Ni−6Cr−7Mn alloy might be caused by Ni_3Mn phase [8] or DO_{22} and $L1_2$ structures produced by the spinodal decomposition [30]. The orientation relationship between the DO_{22} and $L1_2$ ordered phases and the matrix was found to be

$$(020)_{Cu}//(010)_{L1_2},\ [100]_{Cu}//[100]_{L1_2};$$

$$(020)_{Cu}//(2\bar{2}0)_{DO_{22}},\ [100]_{Cu}//[11\bar{1}]_{DO_{22}}.$$

The TEM images of the Cu−19Ni−6Cr−7Mn alloy aged for 5 min at 500 °C are shown in Fig. 10. Figures 10(a, b) show the BF, HRTEM, and FFT images of the acicular precipitates (ordered phase), which contained the DO_{22} diffraction spots that confirmed the presence of the DO_{22} ordered phases.

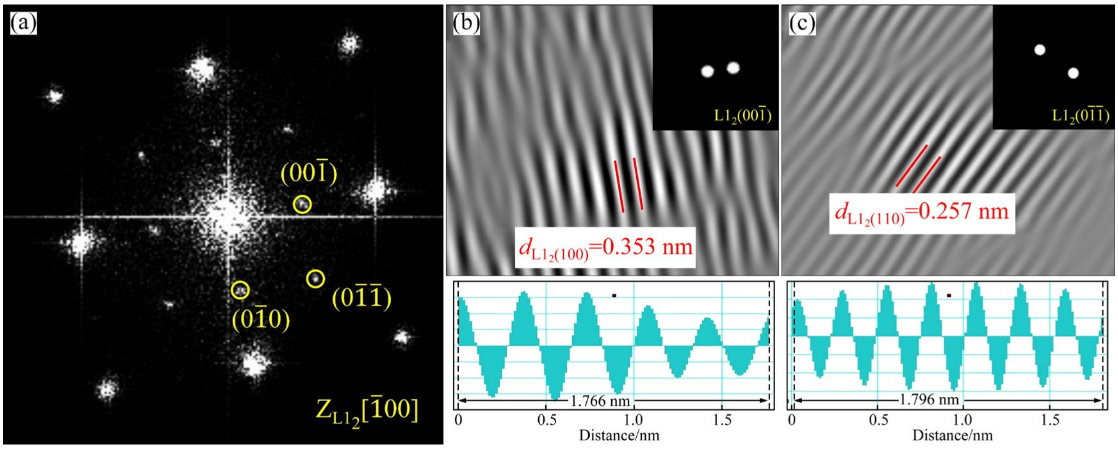

Fig. 9 FFT and IFFT diagram of $L1_2$ superlattice diffraction spots and measurement results of crystal plane spacing: (a) FFT diagram of $L1_2$; (b) IFFT diagram of $L1_2$ in $(00\bar{1})$ direction; (c) IFFT diagram of $L1_2$ in $(0\bar{1}\bar{1})$ direction

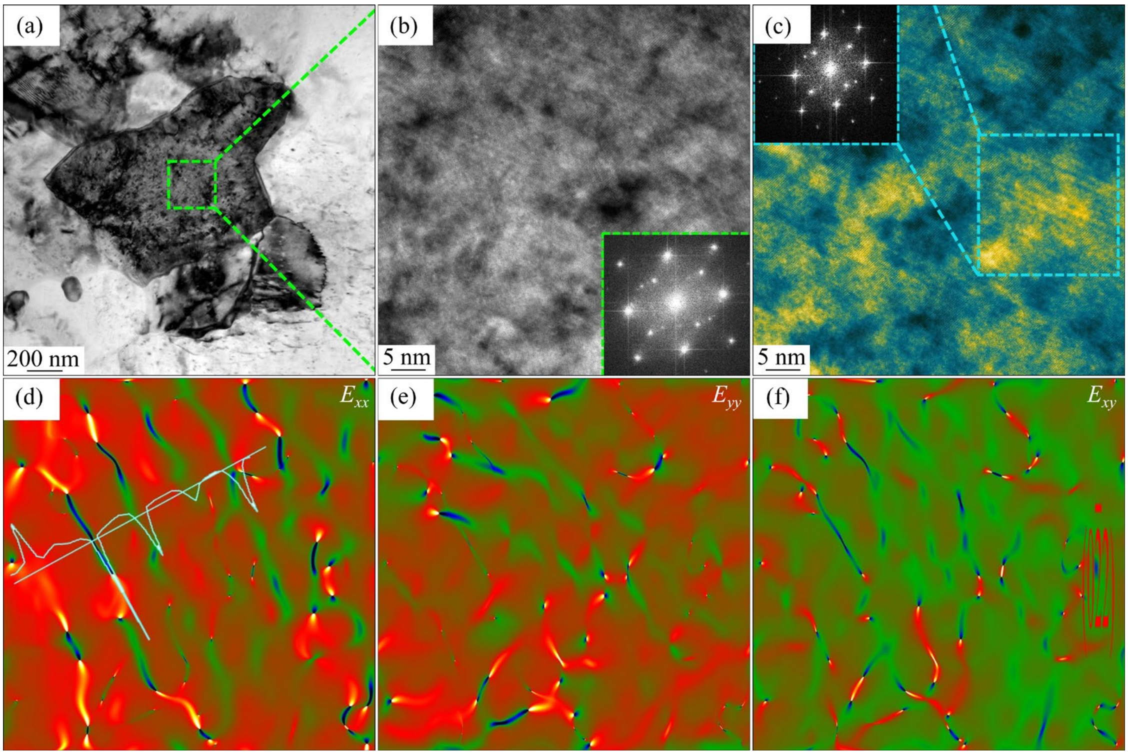

Fig. 10 Detailed TEM analysis of Cu−19Ni−6Cr−7Mn alloy aged at 500 °C for 5 min showing strain state: (a) BF image; (b) HRTEM image of green box area in (a); (c) Stained picture of (b); (d) Horizontal normal strain, E_{xx}; (e) Vertical normal strain, E_{yy}; (f) Shear strain, E_{xy}

The HRTEM image in Fig. 10(c) shows the DO_{22} ordered phase region, which had a distinct wavy striped structure under alternating light and dark conditions. A geometric phase analysis (GPA) of this region was conducted, as shown in Figs. 10(d−f). The alternating strain fields of the stretched and compressed atoms in the matrix are shown in Fig. 10(d). These periodic elastic stress fields could impede dislocations, thereby increasing the tensile strength and elastic modulus of the matrix [31].

The TEM images of the Cu−19Ni−6Cr−7Mn alloy aged for 120 min at 500 °C are shown in Fig. 11. The matrix species exhibited significant Cr-rich precipitates and numerous dislocation lines, tangles, and pile-ups (Figs. 11(a, b)). After aging for 120 min at 500 °C, recovery and recrystallization did not reduce the number of dislocations in the matrix. The EDS elemental distributions corresponding to Fig. 11(b), shown in Figs. (b_1−b_4), revealed that numerous smaller bcc-Cr phaes precipitated from the alloy. The BF images of these phases are shown in Fig. 11(c). The HRTEM and FFT images of the precipitated particles and matrix are shown in Fig. 11(d). The FFT images showed the superlattice spots corresponding to the $L1_2$ ordered phase, which confirmed that a precipitated phase with an $L1_2$ structure was present. No superlattice diffraction spots corresponding to the DO_{22} phase were found, which suggested that the DO_{22} phase completely transformed to the $L1_2$ phase after aging for 120 min at 500 °C.

The TEM images of the Cu−19Ni−6Cr−7Mn alloy aged for 120 min at 700 °C are shown in Fig. 12. As shown in Fig. 12(a), the coarsening occurred after aging, most of the dislocations in the matrix were annihilated, and the precipitated phase grew. The EDS elemental distribution and statistical results for the size and quantity distribution of the precipitated phase are shown in Figs. 12(a_1−a_4) and 13, respectively. After aging, the size of the bcc-Cr particles increased significantly. The BF and SAED images (Fig. 12(b)) showed a Cr-rich particles with a grain diameter of ~714.9 nm, which confirmed the existence of the Cr-rich particles. The BF image of the precipitated bcc-Cr precipitates (Fig. 12(c)) showed the Cr precipitates at the grain boundary. The HRTEM, FFT, and IFFT results revealed the coherent interfaces between the bcc-Cr precipitates and Cu matrix, as shown in Figs. 12(d_1−d_2). In the SAED mode, the aged Cu−19Ni−6Cr−7Mn alloy exhibited a diffraction pattern corresponding to the

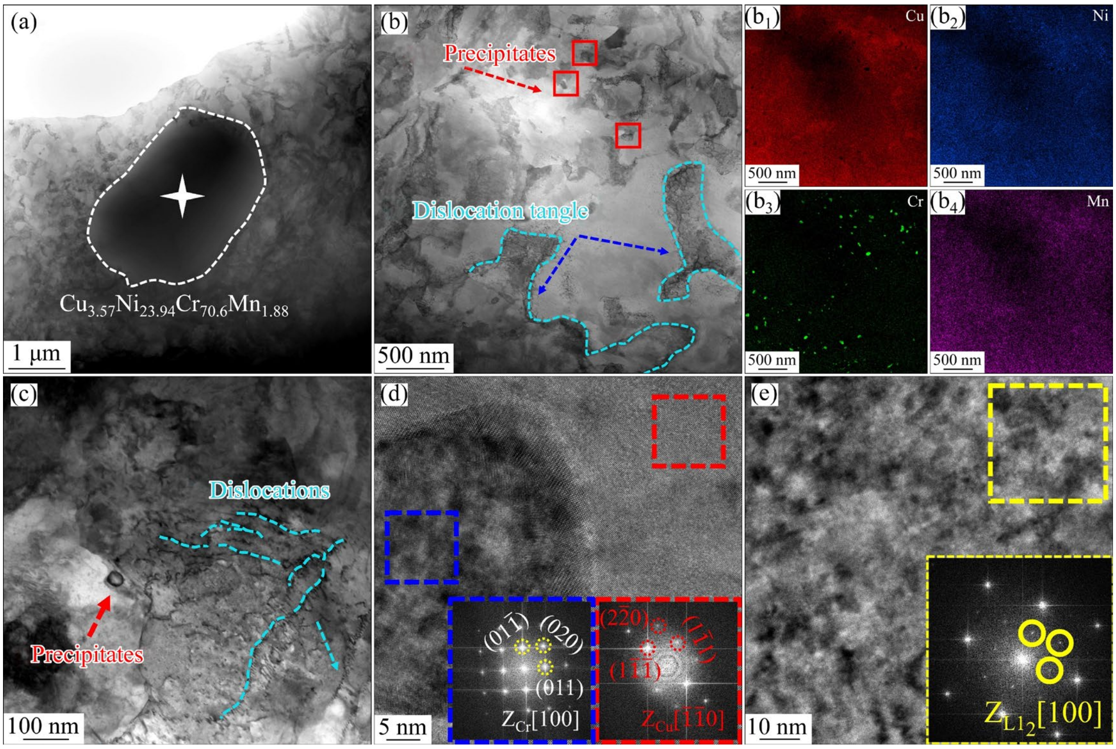

Fig. 11 TEM analysis of Cu−19Ni−6Cr−7Mn alloy aged at 500 °C for 120 min: (a, c) BF images; (b) Low power BF image; (b_1−b_4) EDS element distribution in (b); (d) HRTEM and FFT images of precipitates; (e) HRTEM image of matrix and superlattice diffraction spots

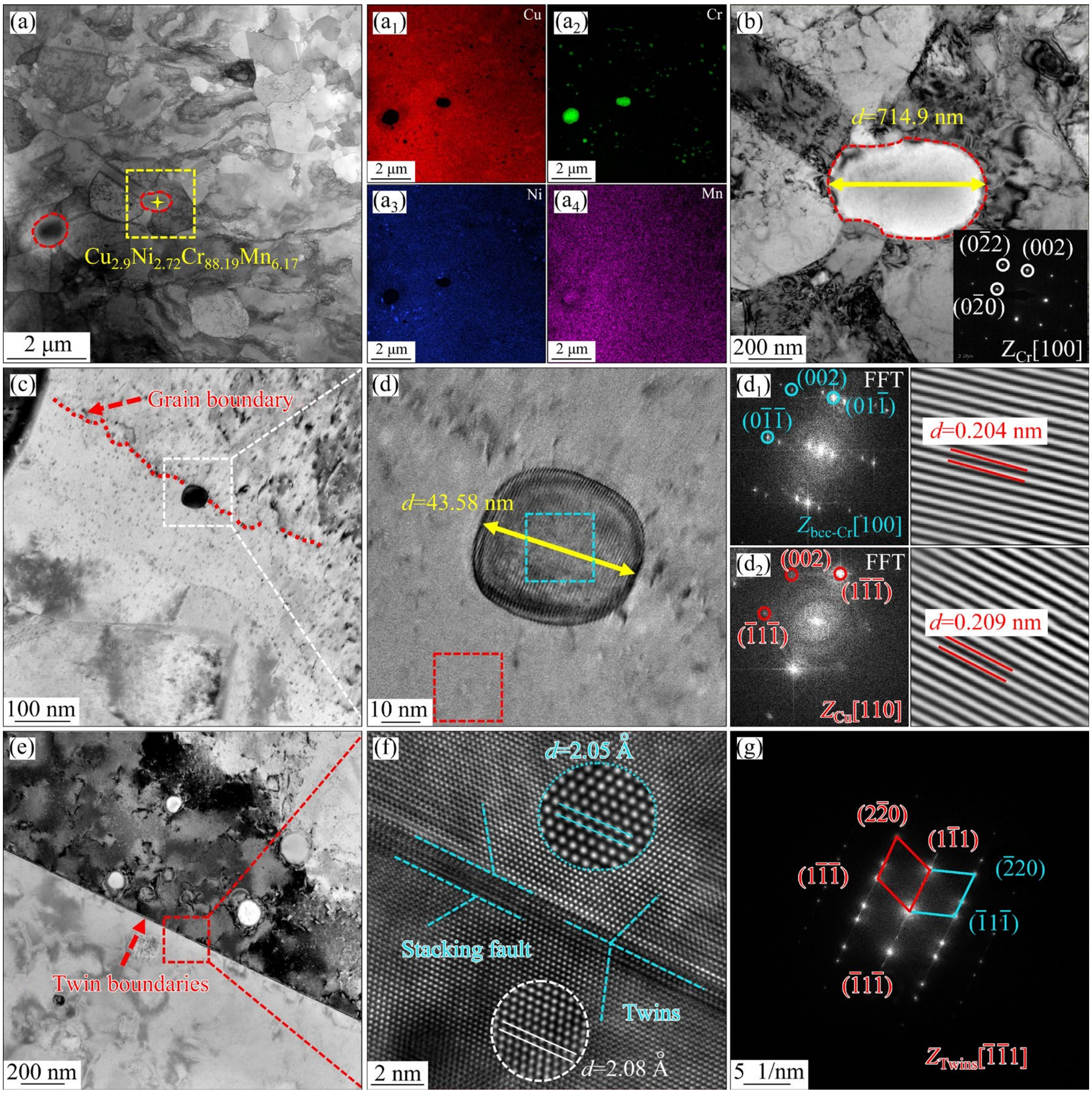

Fig. 12 TEM analysis of Cu−19Ni−6Cr−7Mn alloy aged at 700 °C for 120 min: (a, b) BF images; (a_1−a_4) EDS element distribution in (a); (c) BF image of precipitates; (d) Enlarged HRTEM image of precipitates in (c); (d_1, d_2) FFT and IFFT images corresponding to blue and red areas in (d), respectively; (e) BF image of twin boundary; (f) HRTEM image of crystal structure; (g) FFT image of (f)

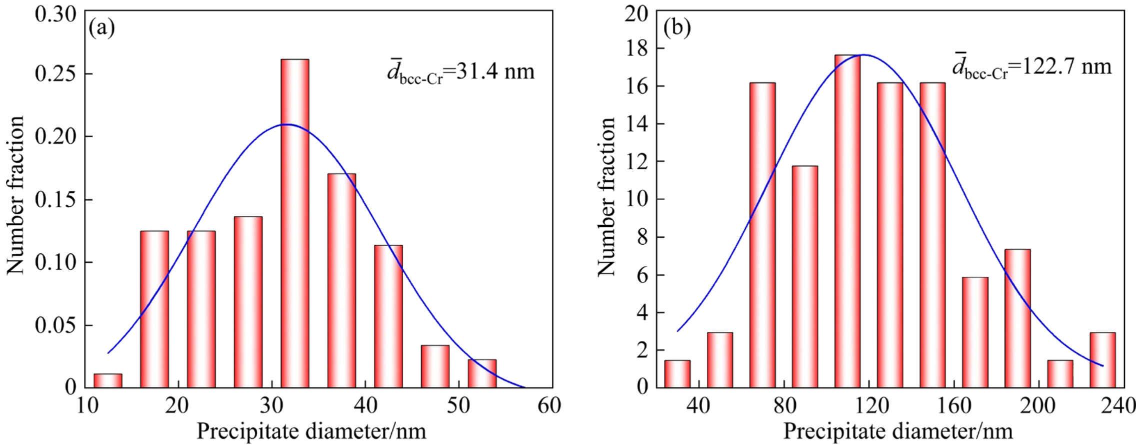

Fig. 13 Size distributions of precipitated phase of aged Cu−19Ni−6Cr−7Mn alloy: (a) 500 °C, 5 min; (b) 700 °C, 120 min

Cu matrix and no superlattice diffraction was detected, which indicated that $L1_2$ ordered phase was dissolved in the matrix. The XRD results in Fig. 4 indicated that the Ni_3Mn precipitates disappeared after aging at for 120 min at 700 °C, which suggested that the Ni_3Mn precipitates with an $L1_2$ structure formed a solid solution with the matrix. These findings were consistent with the TEM results. The twin boundary and HRTEM image are shown in Figs. 12(e, f), respectively. The FFT image in Fig. 12(g) showed a symmetrically distributed electron diffraction pattern, a characteristic of twinned crystals. The coherent twinned structure, confirmed by the interplanar spacing measurements, could store dislocations, which improved the strain-hardening ability and elongation of the alloy [32].

4 Discussion

4.1 Aging precipitation kinetics of Cu−19Ni−6Cr−7Mn alloy

The conductivity of the Cu−19Ni−6Cr−7Mn alloy increased during aging owing to the change in the number of dissolved alloy atoms and the proportion of precipitates. Precipitation kinetics are typically investigated through the resistivity measurement, which indicates a proportional relationship between the conductivity and volume fraction of the precipitated phase of Cu alloys [33,34]. In this study, the aging kinetics equation for Cu−19Ni−6Cr−7Mn was derived using the conductivity after isothermal aging at 500 °C. The electrical conductivity is linearly proportional to the number of integrals of the precipitated objects, which can be expressed as follows [35]:

$$\sigma=\sigma_0+Af \qquad (2)$$

where σ_0 is the initial conductivity of the alloy before aging, σ is the conductivity after a given aging time, A is the difference between the maximum conductivity after aging and the initial conductivity ($A=\sigma_{\mathrm{MAX}}-\sigma_0$), and f is the volume fraction of precipitated phase.

Aging time t and volume fraction f conform to Avrami's empirical equation for the dynamics of phase transitions [36]. That is,

$$f=1-\exp(-bt^n) \qquad (3)$$

where b and n are constants; b is related to the phase transition temperature and the original composition of the solid solution and n is related to the grain shape, which is related to the phase transition and nucleation modes and can indicate boundaries (n=1), edges (n=2), and angles (n=3). When $n<1$, the precipitated phase undergoes uniform nucleation within the matrix. Taking the logarithm of both sides of Eq. (3) gives

$$\ln[\ln 1/(1-f)]=n\ln t+\ln b \qquad (4)$$

According to Eq. (4), a linear graph of $\ln[\ln 1/(1-f)]$ can be used to obtain the values of b and n, as shown in Fig. 14(a). Thus, b and n were determined to be 2.28 and 0.1, respectively. The variation in f with the aging time can be determined by fitting the conductivity value. The values of b and n in the transformation kinetic equation for Cu−19Ni−6Cr−7Mn alloy after aging at 400, 500, 600, and 700 °C are listed in Table 3.

Table 3 Values of b and n in transformation kinetic equation for Cu−19Ni−6Cr−7Mn alloy

Aging temperature/°C	b	n
400	0.28	0.35
500	2.28	0.1
600	0.37	0.32
700	0.13	0.5

The relationship between the volume fraction of the precipitated phase at 500 °C and aging time is shown in Fig. 14(b). The precipitation rate initially increased sharply, and then gradually decreased and stabilized. This was primarily caused by the supersaturation of matrix during early aging, which is the main driving force for precipitation. Upon prolonged aging, the concentration of solute elements in the solid solution decreased, which weakened the driving force for nucleation [5]. The volume fraction of the precipitated phase in the Cu−19Ni−6Cr−7Mn alloy was high, reaching 93.13% after aging for 5 min at 500 °C; this indicates that the properties of the alloy were improved rapidly.

4.2 Strengthening mechanism of Cu−19Ni−6Cr−7Mn alloy aged for 5 min at 500 °C

The yield strength of an alloy is typically defined by four strengthening mechanisms:

$$\sigma_{\mathrm{all}}=\sigma_0+\Delta\sigma_{\mathrm{ss}}+\Delta\sigma_{\mathrm{d}}+\Delta\sigma_{\mathrm{gb}}+\Delta\sigma_{\mathrm{p}} \qquad (5)$$

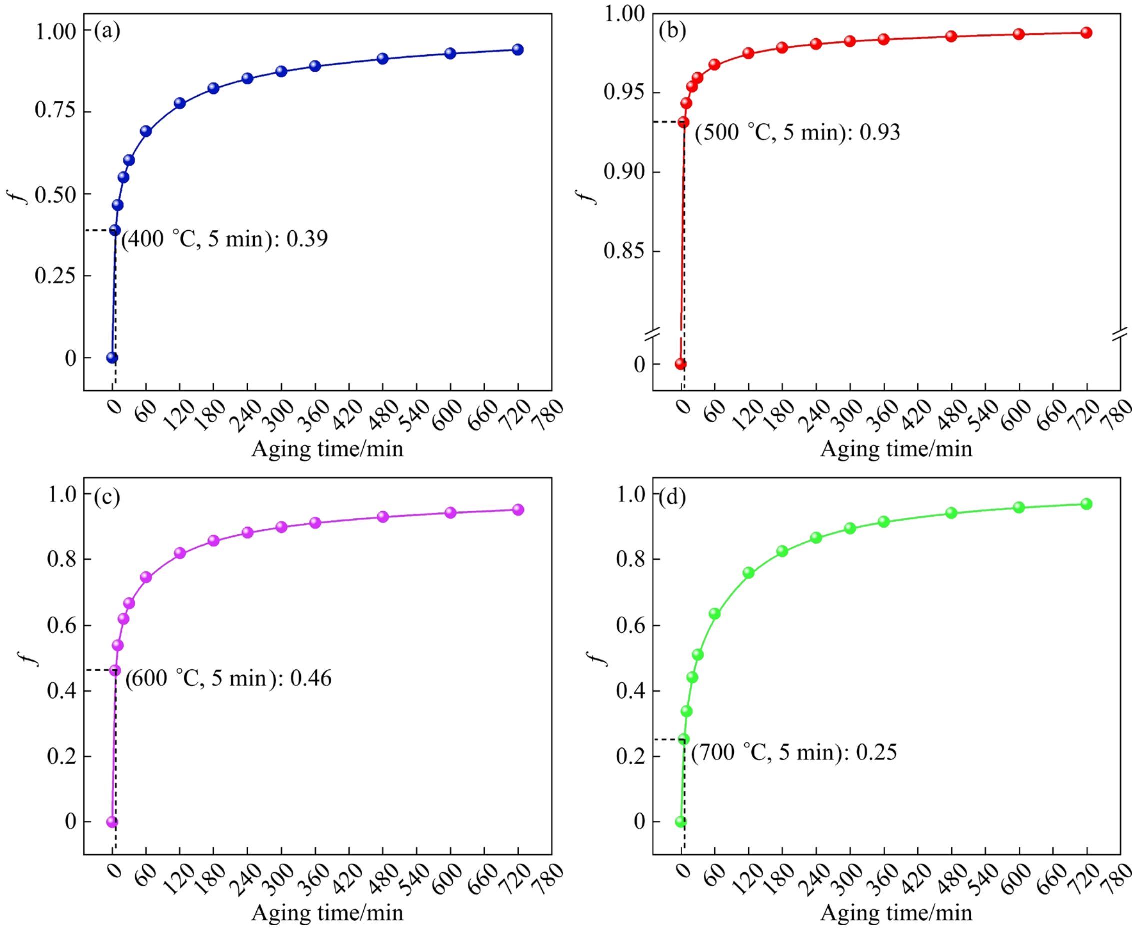

Fig. 14 Aging kinetics curves of Cu−19Ni−6Cr−7Mn alloys: (a) 400 °C; (b) 500 °C; (c) 600 °C; (d) 700 °C

where σ_{all} is the total yield strength of the alloy, σ_0 is the yield strength of annealed Cu (σ_0=40 MPa [28]), $\Delta\sigma_{ss}$ is the solid solution reinforcement, $\Delta\sigma_d$ is the dislocation strengthening, $\Delta\sigma_{gb}$ is grain boundary reinforcement, and $\Delta\sigma_p$ is the precipitation strengthening.

4.2.1 Solid-solution strengthening

At high temperatures, Cu and Ni in the Cu−19Ni−6Cr−7Mn alloy are miscible and can form an infinite solid solution, and Mn can be dissolved in Cu to a large extent, which strengthens the alloy. Solid-solution strengthening ($\Delta\sigma_{ss}$) can be expressed as [35]

$$\Delta\sigma_{ss}=MG\varepsilon_{ss}^{3/2}c^{1/2}/700 \tag{6}$$

where M is the Taylor factor of the Cu matrix (3.06); G is the shear modulus of the Cu alloy (46 GPa); ε_{ss} is the mismatch strain; c is the mass fraction of the Ni and Mn atoms (19.34 wt.% + 7.18 wt.%, in this study). At room temperature (~25 °C), the solid solubility of Cr was much lower than that of Ni and Mn. Therefore, the increase in the strength of Cr was considered to be insignificant. The strength increments due to the Ni and Mn atoms in the Cu−19Ni−6Cr−7Mn alloy were 108.2 and 66 MPa, respectively.

4.2.2 Dislocation strengthening

Dislocations provide a path for the short-circuit diffusion of solute atoms, which accelerates the precipitation of bcc-Cr and ordered phases [36]. Dislocation strengthening ($\Delta\sigma_d$) can be estimated using the Taylor relation [37]:

$$\Delta\sigma_d=M\alpha Gb\rho^{1/2} \tag{7}$$

where α is a constant (0.2); b is the magnitude of Burgers vector of the Cu matrix (0.2556 nm). Moreover, ρ is the dislocation density, which can be determined using the equation [38,39]:

$$\rho=16.1\varepsilon^2/b^2 \tag{8}$$

where ε is the microstrain, which can be obtained from the XRD results using the Williamson–Hall plot method.

4.2.3 Grain boundary strengthening

Grain boundary strengthening ($\Delta\sigma_{\text{gb}}$) can be expressed using the Hall–Petch equation [40]:

$$\Delta\sigma_{\text{gb}}=kD^{-1/2} \tag{9}$$

where k is a constant for Cu alloys (140 MPa·m^2) [41] and D is the average diameter of the grains (determined to be 1.13 μm based on the TEM images using the conventional intercept method).

4.2.4 Precipitation strengthening

The deformation and softening form fine precipitates, which obstruct dislocation movement and increase the alloy strength [42]. The bcc-Cr precipitates are harder than the Cu matrix. The size of the ordered phase exceeded the critical phase size; therefore, its yield strength contribution was calculated on the basis of the Orowan mechanism. The Orowan strengthening contribution can be calculated using Eq. (10) [43,44]:

$$\Delta\sigma_{\text{p}}=M\frac{0.4}{\pi}\frac{Gb}{\sqrt{1-v}}\frac{1}{\lambda}\ln\left[\frac{2(\sqrt{2/3}r)}{b}\right] \tag{10}$$

$$\lambda=\left(\sqrt{(3\pi)/(4f)}-1.64\right)r \tag{11}$$

$$f=\left(N/S\right)^{3/2}1/6\pi\bar{d}^3 \tag{12}$$

where v is Poisson's ratio (0.34); r is the radius of the bcc-Cr precipitates ($r=1/2\bar{d}$ and $\bar{d}$=31.4 nm, as shown in Fig. 11(a)); λ is the spacing of the precipitate precipitates. Moreover, S is the measurement area and N is the number of the precipitated phases in TEM images (Figs. 8(b$_3$, f)). The calculation based on Eqs. (10)−(12) shows that the strength contributions of the bcc-Cr precipitates and the DO$_{22}$ and L1$_2$ ordered phases relative to the matrix were 281.1 and 158.6 MPa, respectively.

Figure 15 shows the strength contributions from each mechanism and compares the calculated and measured tensile strengths. The measured tensile strength of the Cu−19Ni−6Cr−7Mn alloy was 806 MPa, and the theoretical contributions from precipitation, solid-solution, grain-boundary, and dislocation strengthening were 439.7, 174.2, 131.7, and 78.9 MPa, respectively. The actual calculated strength slightly exceeded the theoretical value, mainly due to the statistical errors when determining the precipitated phase size and quantity [45]. These findings indicate that precipitation strengthening is the primary strengthening mechanism during short-term aging at 500 °C. The bcc-Cr precipitates, L1$_2$ ordered phase, and spinodal decomposition of the DO$_{22}$ ordered phase collectively improve the mechanical properties of the alloy.

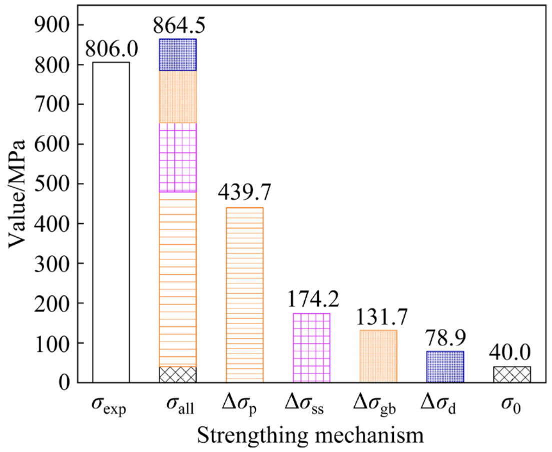

Fig. 15 Contribution of strengthening mechanisms to strength of Cu−19Ni−6Cr−7Mn alloy aged at 500 °C for 5 min

4.3 Strengthening mechanism of Cu−19Ni−6Cr−7Mn alloy after short time aging

The microstructures and properties of the Cu−19Ni−6Cr−7Mn alloy aged at various temperatures for different durations were investigated. Optimum results were achieved after aging for 120 min at 500 °C. In the first 5 min of aging at 500 °C, the tensile strength of the Cu−19Ni−6Cr−7Mn alloy increased rapidly from 740 to 934 MPa, which was only 43 MPa lower than the maximum tensile strength achieved under the optimum aging conditions. The mechanical properties of the Cu−19Ni−6Cr−7Mn alloy improved quickly during the early stage of aging, which is characteristic of spinodal decomposition. The periodic elastic stress field from component fluctuations by spinodal decomposition causes dislocation distortion, which leads to a sharp increase in the mechanical properties during the early stage of aging [2]. This study focused on the microstructural evolution during short-term aging for 5 min at 500 °C with the aim of clarifying the correlation between the microstructure and properties of the Cu−19Ni−6Cr−7Mn alloy.

The mechanical properties and electrical conductivity of the Cu−19Ni−6Cr−7Mn alloy aged at 500 °C for various durations are shown in Fig. 3. After aging for 5 min at 500 °C, the tensile strength of the alloy reached 934 MPa, which was only 4.5%

lower than the maximum value achieved under the optimum aging conditions. After aging for 3000 min, the strength of the Cu−19Ni−6Cr−7Mn alloy remained at 800 MPa, which surpassed that of the cold-rolled alloy (740 MPa). Among the alloy aged for 60−300 min at 500 °C, the maximum elastic modulus of 149.5 GPa was achieved after 240 min. This is one of the highest values reported for Cu alloys.

The TEM analysis (Figs. 7−12) revealed a strong correlation between the properties of the Cu−19Ni−6Cr−7Mn alloy and the formation and growth of the precipitated phases during aging. During the early stage of aging, the strength of the Cu−19Ni−6Cr−7Mn alloy increased rapidly owing to Cu matrix supersaturation and spinodal decomposition, which prompted precipitation. Aging for 5 min at 500 °C resulted in superlattice spots, which indicated the presence of the DO_{22} ordered phase in the matrix. This is evidence of phase separation and DO_{22} ordering during spinodal decomposition. This ordered phase precipitation involves a two-stage transformation of spinodal decomposition initiation followed by structural ordering/disordering [16]. The periodic distribution of spinodal decomposition structures significantly improves the mechanical properties of the Cu−19Ni−6Cr−7Mn alloy through strengthening effects [46]. Cu−Ni−Sn alloys decompose rapidly during the early stage of aging at 400 °C [47] and WANG [48] showed that spinodal decomposition occurred after aging for just 10 s. The TEM images showed DO_{22} ordered spots when Cu−19Ni−6Cr−7Mn alloy was aged for 5 min at 500 °C, which indicates that spinodal decomposition occurred. The time of spinodal decomposition was calculated using the equations [46,49]:

$$t_1 = \lambda_1^2 / (12|D_1|) \tag{13}$$

$$\lambda_1 = [(ha_0)/(h^2+k^2+l^2)] \cdot [\tan\theta/\Delta\theta] \tag{14}$$

where t_1 is the time of spinodal decomposition; λ_1 is the wavelength of the spinodal decomposition structure, which can be estimated using the Daniel−Lipson formula [15]; a_0 is the lattice parameter (3.615 nm); (hkl) is the Miller index. In this study, based on (220), θ is the Bragg diffraction angle and $\Delta\theta$ is the distance between the diffraction peak side and the diffraction peak. Moreover, D_1 is the diffusion coefficient of the solute atoms, which is 6.8×10^{-19} m^2/s [50]. Thus, the spinodal-resolution wavelength of the Cu−19Ni−6Cr−7Mn alloy was ~11.2 nm and the time of spinodal decomposition was ~15 s. The Cu−19Ni−6Cr−7Mn alloy aged for approximately 15 s possessed the spinodal decomposition structure. The TEM results showed that after aging for 5 min, the DO_{22} ordered transformation occurred during the spinodal decomposition. Simultaneously, many small and dispersed bcc-Cr precipitates were rapidly generated within the matrix, and the $L1_2$ ordered phases were observed. The bcc-Cr precipitates, DO_{22} ordered phase, and $L1_2$ ordered phase were completely coherent with the matrix, which significantly improved the mechanical properties of the Cu−19Ni−6Cr−7Mn alloy [51].

The transformation sequence of the Cu−15Ni−8Sn alloy involved the spinodal decomposition structure, the DO_{22} ordered phase, co-existing DO_{22} and $L1_2$ ordered phases, and the transformation of the DO_{22} to $L1_2$ ordered phase [30]. In Cu−15Ni−8Sn−0.2Nb aged at 400 °C, spinodal decomposition, DO_{22}/$L1_2$ ordered phases, and a discontinuous precipitated phase were observed [46]. Furthermore, as shown in Fig. 11, the number of bcc-Cr precipitates increased with prolonged aging of 120 min at 500 °C. The corresponding TEM image (Fig. 7) only showed superlattice spots corresponding to the $L1_2$ ordered phase in the matrix, and no DO_{22} phase spots were observed.

The Cu−Ni−Cr alloy considered in this study is a typical spinodal decomposition alloy, in which the oversaturated solid-solution phases decompose and form ordered phases during aging. Over time, the nanoparticles become ordered and transition from the DO_{22} to $L1_2$ phase appears. During nanoparticle formation, chemical segregation and structural ordering occur sequentially [52]. The Cu−19Ni−6Cr−7Mn alloy containing Mn element precipitated $L1_2$ ordered phases during aging. Therefore, further investigations are required to understand the spinodal decomposition evolution in this alloy. Both the $L1_2$ and DO_{22} phases are coherently related to the matrix, which improves the mechanical properties of the alloy [53].

When the aging temperature and aging time increased to 700 °C and 120 min, respectively, the bcc-Cr precipitates coarsened and lost coherence with the matrix. The XRD and TEM results revealed no diffraction peaks or superlattice points for the $L1_2$ ordered phase at 700 °C, due to the redissolution of the Ni_3Mn precipitates into the Cu matrix as the aging temperature increased. The increased spacing between the Ni_3Mn precipitates reduced the dislocation movement resistance and facilitated dislocation slip, thereby reducing the alloy strength and hardness, and increasing plasticity [54]. The aging process involves a balance between precipitation strengthening and recovery softening, in which the dislocation disappearance and precipitate coarsening degrade the mechanical properties.

5 Conclusions

(1) Cu−19Ni−6Cr−7Mn alloy achieved peak hardness (HV 375.5) after aging for 120 min at 500 °C, and the corresponding tensile strength and elastic modulus were 978 MPa and 145.8 GPa, respectively. Notably, after short-term aging for 5 min at 500 °C, the tensile strength of the alloy increased to 934 MPa rapidly. After aging for 240 min at 500 °C, the elastic modulus of the Cu−19Ni−6Cr−7Mn alloy reached 149.5 GPa, which is one of the highest values reported for Cu alloys.

(2) At aging temperatures of 400 and 500 °C, the Ni_3Mn precipitates in the Cu−19Ni−6Cr−7Mn alloy gradually precipitated from the matrix. At aging temperatures of 600 and 700 °C, the Ni_3Mn precipitates redissolved into the matrix, the $L1_2$ ordered phase diffraction spots disappeared, and significant coarsening of the bcc-Cr precipitates occurred.

(3) The Cu−19Ni−6Cr−7Mn alloy underwent precipitation hardening after a short aging time of 5 min, which improved the mechanical properties through a combination of precipitation strengthening, solid-solution strengthening, and deformation strengthening. The main strengthening mechanism in the alloy was precipitation strengthening owing to the spinodal decomposition and the presence of nanoscale ordered phase and Cr precipitates. The periodic coherent stress field generated by spinodal decomposition plays a crucial role in determining the mechanical properties of the alloy.

CRediT authorship contribution statement

Shao-lin LI: Supervision, Funding acquisition, Writing − Review & editing; **Ying-ying ZHU:** Conceptualization, Methodology, Formal analysis, Writing − Original draft; **Xiu-hua GUO:** Formal analysis, Investigation, Writing − Review & editing; **Qiang-song WANG:** Supervision, Funding acquisition, Writing − Review & editing; **Wen-ming SUN:** Formal analysis, Investigation, Writing − Review & editing; **Ke-xing SONG:** Formal analysis, Investigation, Writing − Review & editing.

Declaration of competing interest

The authors declare that they have no known competing financial interests or personal relationships that could have appeared to influence the work reported in this paper.

Data availability

The raw/processed data required to reproduce these findings cannot be shared at this time as the data also forms part of an ongoing study.

Acknowledgments

This work was supported by the National Key R&D Program of China (No. 2021YFB3700700), the Henan Province Top Talent Training Program Project, China (No. 244500510020), and the High-level Talent Research Start-up Project Funding of Henan Academy of Sciences, China (No. 242017001).

References

[1] LI Jia-zhi, DING Hua, LI Bao-mian. Study on the variation of properties of Cu−Cr−Zr alloy by different rolling and aging sequence [J]. Materials Science and Engineering A, 2021, 802: 140413.

[2] WANG Guo-jie, LIU Hai-tao, SONG Ke-xing, ZHOU Yan-jun, CHENG Chu, GUO Hui-wen, GUO Yin-gang, TIAN Jing. Aging process and strengthening mechanism of Cu−Cr−Ni alloy with superior stress relaxation resistance [J]. Journal of Materials Research and Technology, 2022, 19: 3579−3591.

[3] YANG Kuo, WANG Yi-han, GUO Ming-xing, WANG Hu, MO Yong-da, DONG Xue-guang, LOU Hua-fen. Recent development of advanced precipitation-strengthened Cu alloys with high strength and conductivity: A review [J]. Progress in Materials Science, 2023, 138: 101141.

[4] ZHAO Chao, WANG Zhi, PAN De-qing, LI Dao-xi, LUO Zong-qiang, ZHANG Da-tong, YANG Chao, ZHANG Wei-wen. Effect of si and ti on dynamic recrystallization of high-performance Cu−15Ni−8Sn alloy during hot deformation [J]. Transactions of Nonferrous Metals Society of China, 2019, 29: 2556−2565.

[5] WANG Nan, SHEN Yi-di, AN Qi, REDDY K M, JIN Ming-jiang, KARRE R, WANG Xiao-dong. Microstructure evolution and mechanical property of Cu−15Ni−8Sn−0.2Nb alloy during aging treatment [J]. Journal of Materials Science & Technology, 2021, 86: 227−236.

[6] WENG Yuan-hui, LIU Yuan-xuan, WEI Tan, ZHANG Wei-wen, LUO Zong-qiang. Influence of extrusion ratio on microstructures and properties of Cu−17Ni−3Al−X alloy [J]. Applied Mechanics and Materials, 2014, 477/478: 1307−1315.

[7] LI Z M, MENG W L, HU Y L, ZHENG Y H, LIU R W, LI J S, LIU T, LIU Q, LI X N. Differential effects of Sn and Si solutes on the microstructure and properties of Cu−Ni−Al alloys with coherent $L1_2$-γ' phases [J]. Vacuum, 2023, 215: 112355.

[8] LIU Bin, ZHAO Ge-ying, ZHANG Xin-bin, GUO Jia-li, GONG Shen, XIE Guo-liang, PENG Li-jun, LI Zhou. High-temperature deformation behavior of a novel high strength and high elasticity Cu−20Ni−20Mn−0.3Nb−0.3Cr−0.1Zr alloy [J]. Intermetallics, 2021, 132: 107162.

[9] HUANG Song-wei, ZHOU Peng-fei, LUO Fu-xin, CHEN Hui-ming, XIE Wei-bin, ZHANG Wen-jing, WANG Hang, YANG Bin, PENG Bing-feng. Effects of Ni and Mn contents on precipitation and strengthening behavior in Cu−Ni−Mn ternary alloys [J]. Materials Characterization, 2023, 199: 112775.

[10] LI Cong, WANG Xian-hui, LI Bo, SHI Jing, LIU Yan-feng, XIAO Peng. Effect of cold rolling and aging treatment on the microstructure and properties of Cu−3Ti−2Mg alloy [J]. Journal of Alloys and Compounds, 2020, 818: 152915.

[11] WEI Huan, CUI Yan-chao, CUI Hui-qi, WEI Ying-hui, HOU Li-feng. Effects of multiple trace alloying elements on the microstructure and properties of Cu−4wt.%Ti alloys [J]. Materials Science and Engineering A, 2017, 707: 392−398.

[12] LI X N, LI Z M, CHENG X T, SUN W, ZHENG Y H, YU Q X, WANG C Y, WANG Q, DONG C. Precipitation evolution in $Cu_x[Ni_3Cr_1]$ spinodal alloys under mismatch control [J]. Materials Chemistry and Physics, 2019, 223: 486−493.

[13] CHOU A, DATTA A, MEIER G H, SOFFA W A. Microstructural behaviour and mechanical hardening in a Cu−Ni−Cr alloy [J]. Journal of Materials Science, 1978, 13: 541−552.

[14] LOPEZ-HIRATA V M, HERNÁNDEZ-SANTIAGO F, DORANTES-ROSALES H J, SAUCEDO-MUÑOZ M L, HALLEN-LOPEZ J M. Phase decomposition during aging for Cu−Ni−Cr alloys [J]. Materials Transactions, 2001, 42: 1417−1422.

[15] FINDIK F. Modulated structures in Cu−32Ni−3Cr and Cu−46Ni−17Cr alloys [J]. Canadian Metallurgical Quarterly, 2002, 41: 337−347.

[16] FINDIK F, FLOWER H M. Morphological changes and hardness evolution in Cu−30Ni−5Cr and Cu−45Ni−15Cr spinodal alloys [J]. Materials Science and Technology, 1993, 9(5): 408−416.

[17] SUN Wen-ming, LI Shao-lin, SONG Ke-xing, WANG Qiang-song, ZHU Ying-ying. Effects of cold rolling reduction rate on the microstructure and properties of Cu−1.16Ni−0.36Cr alloy after thermo-mechanical treatment [J]. Materials, 2023, 16(9): 6508.

[18] LI Shao-lin, SUN Wen-ming, SONG Ke-xing, WANG Qiang-song, ZHU Ying-ying. Enhanced high-temperature mechanical properties of the Cu−1.16Ni−0.36Cr alloy owing to interactions between metastable precipitates and dislocations [J]. Journal of Materials Research and Technology, 2024, 29: 2999−3010.

[19] ZOU J T, ZHAO J P, WANG Xian-hui, LIANG S H. Effect of trace boron addition on microstructure and properties of cunimnfe alloy [J]. The Chinese Journal of Nonferrous Metals, 2013, 23: 1005−1011. (in Chinese)

[20] MA Mu-zhi, XIAO Zhu, MENG Xiang-peng, LI Zhou, GONG Shen, DAI Jie, JIANG Hong-yun, JIANG Yan-bin, LEI Qian, WEI Hai-gen. Effects of trace calcium and strontium on microstructure and properties of Cu−Cr alloys [J]. Journal of Materials Science & Technology, 2022, 112: 11−23.

[21] GUO Cheng-jun, SHI Yu-fan, SHEN Shou-wen, LI Zhi-guo, HU Zhi-jun, GONG Ya-hui, XIAO Xiang-peng, YANG Bin. Microstructural changes and dry sliding wear behavior of Cu−15Ni−8Sn−0.5Co alloy during deformation and aging treatment [J]. Materials Today Communications, 2024, 38: 107961.

[22] HUANG Lue, PENG Li-jun, MI Xu-jun, ZHAO Gang, HUANG Guo-jie, XIE Hao-feng, ZHANG Wen-jing. Relationship between microstructure and properties of high-strength Cu−Ti−Cr alloys during aging [J]. Journal of Alloys and Compounds, 2023, 942: 168865.

[23] CHENG J Y, TANG B B, YU F X, SHEN B. Evaluation of nanoscaled precipitates in a Cu−Ni−Si−Zr alloy during aging [J]. Journal of Alloys and Compounds, 2014, 614: 189−195.

[24] LIU Bin, LIU Jin-long, LIU Yan-ting, GONG Shen, DAI Yan-rui, ZHAO Ge-ying, XIE Guo-liang, PENG Li-jun, LI Zhou. Effects of al addition on corrosion behavior and mechanical property of high-strength and high-elasticity Cu−20Ni−20Mn−0.3Nb−0.3Cr−0.3Zr alloy [J]. Materials Characterization, 2020, 167: 110476.

[25] GUO Zhong-kai, JIE Jin-chuan, LIU Shi-chao, ZHANG Yu-bo, QIN Bai-liang, WANG Tong-min, LI Ting-ju. Effect of V addition on microstructures and mechanical properties of Cu−15Ni−8Sn alloy [J]. Materials Science and Engineering A, 2019, 748: 85−94.

[26] SUKHOVA O V. The effect of iron on precipitation hardening in the Cu−Ni−Mn alloys [J]. Physics and Chemistry of Solid State, 2021, 22(3): 487−493.

[27] XIE Guo-liang, WANG Qiang-song, GUO Qing-miao, LIU Dong-mei, XIE Wei-bin, MI Xu-jun, XIONG Bai-qing. Precipitation process and mechanical properties of an elastic Cu−Ni−Mn alloy [J]. Materials Science Forum, 2015, 817: 577−581.

[28] LI Long-jian, KANG Hui-jun, ZHANG Si-ruo, LI Ren-geng, YANG Xiong, CHEN Zong-ning, GUO En-yu, WANG Tong-min. Microstructure and properties of Cu−Cr−Zr (Mg) alloys subjected to cryorolling and aging treatment [J]. Journal of Alloys and Compounds, 2023, 938: 168656.

[29] JIANG Ye-xin, LI Zhou, XIAO Zhu, XING Yan, ZHANG Yang, FANG Mei. Microstructure and properties of a Cu−Ni−Sn alloy treated by two-stage thermomechanical

processing [J]. JOM, 2019, 71: 2734−2741.

[30] GUO Zhong-kai, JIE Jin-chuan, LIU Jia-ming, YUE Shi-peng, LIU Shi-chao, LI Ting-ju. Effect of cold rolling on aging precipitation behavior and mechanical properties of Cu−15Ni−8Sn alloy [J]. Journal of Alloys and Compounds, 2020, 848: 156275.

[31] TU Ying-ming, LIU Xue-feng, WANG Wen-jing, ZHANG Wei-liang, FENG Qi-hang. Deformation-aging behavior and property evolution of Cu−Ti alloys prepared by accumulative roll bonding-deformation diffusion process [J]. Materials Science and Engineering A, 2022, 855: 143915.

[32] JIA LIU, WANG Xian-hui, RAN Qian-ni, GANG ZHAO, ZHU Xiu-xiu. Microstructure and properties of Cu–3Ti–1Ni alloy with aging process [J]. Transactions of Nonferrous Metals Society of China, 2016, 26: 3183−3188.

[33] TANG Yan-chuan, KANG Yong-lin, YUE Li-juan, JIAO Xiao-liang. Precipitation behavior of Cu−1.9Be−0.3Ni−0.15Co alloy during aging [J]. Acta Metallurgica Sinica (English Letters), 2015, 28(3): 307−315.

[34] AVRAMI M. Granulation, phase change, and microstructure kinetics of phase change [J]. Journal of Chemical Physics, 2004, 9(2): 177−184.

[35] YANG Hai-te, WANG Wen-wei-jiao, WANG Chen, WANG Jian, ZHOU Jian-hui, TONG Chang-qing, CHEN Jun-feng, WANG Bing-shu. Effects of aging process on properties and precipitation kinetics of Cu−Cr−Zr alloy strips [J]. Transactions of Nonferrous Metals Society of China, 2023, 33: 2439−2448.

[36] TANG Shun-long, ZHOU Meng, ZHANG Yi, XU Deye, ZHANG Zhi-yang, ZHENG Xian-hua, LI De, LI Xu, TIAN Bao-hong, JIA Yan-lin, LIU Yong, VOLINSKY A A, MARCHENKO E S. Improved microstructure, mechanical properties and electrical conductivity of the Cu−Ni−Sn−Ti−Cr alloy due to Ce micro-addition [J]. Materials Science and Engineering A, 2023, 871: 144910.

[37] SUZUKI S, SHIBUTANI N, MIMURA K, ISSHIKI M, WASEDA Y. Improvement in strength and electrical conductivity of Cu−Ni−Si alloys by aging and cold rolling [J]. Journal of Alloys and Compounds, 2006, 417: 116−120.

[38] WANG Zhang-wei, LU Wen-jun, ZHAO Huan, LIEBSCHER C H, HE Jun-yang, PONGE D, RAABE D, LI Zhi-ming. Ultrastrong lightweight compositionally complex steels via dual-nanoprecipitation [J]. Science Advances, 2020, 6(46): eaba9543.

[39] LIU Wei-jiang, CHEN Xin, AHMAD Tahir, ZHOU Chen-yang, XIAO Xiang-peng, WANG Hang, YANG Bin. Microstructures and mechanical properties of Cu−Ti alloys with ultrahigh strength and high ductility by thermo-mechanical treatment [J]. Materials Science and Engineering A, 2022, 835: 142672.

[40] HANSEN N. Hall−Petch relation and boundary strengthening [J]. Scripta Materialia, 2004, 51: 801−806.

[41] WANG Chang-sheng, FU Hua-dong, ZHANG Hong-tao, HE Xing-qun, XIE Jian-xin. Simultaneous enhancement of mechanical and electrical properties of Cu−Ni−Si alloys via thermo-mechanical process [J]. Materials Science and Engineering A, 2022, 838: 142815.

[42] SUN Xing-long, JIE Jin-chuan, WANG Peng-fei, QIN Bai-liang, MA Xiao-dong, WANG Tong-min, LI Ting-ju. Effects of Co and Si additions and cryogenic rolling on structure and properties of Cu−Cr alloys [J]. Materials Science and Engineering A, 2019, 740/741: 165−173.

[43] COPLEY S M, PASK J A. Plastic deformation of mgo single crystals up to 1600 °C [J]. Journal of the American Ceramic Society, 2010, 48(3): 139−146.

[44] PENG Huai-chao, XIE Wei-bin, CHEN Hui-ming, WANG Hang, YANG Bin. Effect of micro-alloying element Ti on mechanical properties of Cu−Cr alloy [J]. Journal of Alloys and Compounds, 2020, 852: 157004.

[45] QIN Liu-xin, ZHOU Tao, JIANG Xiao-yu, WANG Meng, HU Jin-hui, WU Zi-xiao, MENG Xiang-peng, JIANG Yan-bin, LI Zhou. Microstructure and properties of Cu−Ni−Co−Si−Cr−Mg alloy by multistage thermomechanical treatment [J]. Transactions of Nonferrous Metals Society of China, 2023, 33: 3739−3755.

[46] JIANG Kai-xuan, Zhou Yan-jun, Yang Ran, SONG Ke-xing, LIU Ya-hui, ZHANG Yan-min, YANG Shao-dan, ZHOU Fei, HUANG Kuan, LIU Dong-dong, YANG Wen-hao. Nanophase transformation and strengthening-toughening mechanism of the Cu−15Ni−8Sn alloy during aging [J]. Journal of Materials Research and Technology, 2023, 27: 2201−2215.

[47] ZHAO J C, NOTIS M R. Spinodal decomposition, ordering transformation, and discontinuous precipitation in a Cu−15Ni−8Sn alloy [J]. Acta Materialia, 1998, 46: 4203−4218.

[48] WANG Y H. Phase transformations of Cu−15Ni−8Sn−*x*Si and Cu−9Ni−2.5Sn−1.5A1−0.5Si alloys and their effects on the alloy's properties (phd thesis) [D]. Changsha: Central South University press, 2004. (in Chinese)

[49] SHI Yu-fan, GUO Cheng-jun, CHEN Jin-shui, XIAO Xiang-peng, HUANG Hao, YANG Bin. Recrystallization behavior and mechanical properties of a Cu−15Ni−8Sn(p) alloy during prior deformation and aging treatment [J]. Materials Science and Engineering A, 2021, 826: 142025.

[50] VILJOEN E C, PLESSIS J D, SWART H C, WYK G N. Van. Sn bulk-to-surface diffusion in a Cu(111)(Sn) single crystal [J]. Surface Science, 1995, 342(s1/s2/s3): 1−10.

[51] HUANG Xia-xu, XIE Guo-liang, LIU Xin-hua, FU Hua-dong, SHAO Lei, HAO Zi-fan. The influence of precipitation transformation on young's modulus and strengthening mechanism of a Cu−Be binary alloy [J]. Materials Science and Engineering A, 2020, 772: 138592.

[52] LI W, WANG W, NIU M C, YANG K, LUAN J H, ZHANG H W, JIAO Z B. Unraveling the two-stage precipitation mechanism in a hierarchical-structured fcc/$L2_1$ high-entropy alloy: Experiments and analytical modeling [J]. Acta Materialia, 2024, 262: 119426.

[53] HAO Zi-fan, XIE Guo-liang, LIU Xin-hua, TAN Qing, WANG Rui. The precipitation behaviours and strengthening mechanism of a Cu−0.4wt.%Sc alloy [J]. Journal of Materials Science & Technology, 2022, 98: 1−13.

[54] SHI Lin, ZOU Jun-tao, SUN Li-xing, WANG Yu-xuan, NI Lei, LIANG Shu-hua. Effect of electropulsing treatment on microstructure and mechanical properties of Cu−20Ni−20Mn alloy [J]. Materials Science and Engineering A, 2022, 855: 143847.

基于调幅分解和多尺度析出协同作用的 Cu−19Ni−6Cr−7Mn 合金强化行为

李韶林 [1]，朱莹莹 [1]，国秀花 [1]，王强松 [2,3]，孙文明 [1]，宋克兴 [1,2]

1. 河南科技大学 材料科学与工程学院 河南省有色材料科学与加工技术重点实验室，洛阳 471023；
2. 河南省科学院 材料研究所 河南省先进导体材料重点实验室，郑州 450046；
3. 有研工程技术研究院有限公司，北京 101407

摘　要：研究了 Cu−19Ni−6Cr−7Mn 合金在时效过程中的显微组织演变。结果表明：500 ℃时效 120 min 的合金力学性能最佳，其抗拉强度和弹性模量分别为 978 MPa 和 145.8 GPa。500 ℃时效 240 min 的合金弹性模量达到 149.5 GPa，为目前具有较高弹性模量的铜合金。值得一提的是，500 ℃时效 5 min 的合金其抗拉强度从 740 MPa 迅速升高到 934 MPa，接近最大值 (978 MPa)。对潜在的强化机制和相变行为的分析表明，Cu−19Ni−6Cr−7Mn 合金在 500 ℃时效 5 min 过程中发生调幅分解和 DO_{22} 有序化，并出现 $L1_2$ 有序相和 bcc-Cr 颗粒。调幅分解产生的应力场、纳米级有序相和 Cr 颗粒是 Cu−19Ni−6Cr−7Mn 合金力学性能提高的主要原因。

关键词：Cu−Ni−Cr−Mn 合金；力学性能；纳米析出相；调幅分解；弹性模量

(Edited by Bing YANG)